remote sensing

MDPI

Article

Adaptive Reference Spectrum-Based Spectral and Radiometric Calibration of GF-5B GMI Using Physics-Based Radiative Transfer Simulation

Hailiang Gao [1,2], Ying Li [1,2], Sihan Liu [3,4], Qianqian Wang [1,2], Guimei Gao [3,4,*] and Bingyu Liu [1,2]

[1] Aerospace Information Research Institute, Chinese Academy of Sciences, Beijing 100094, China; gaohl200439@aircas.ac.cn (H.G.); liying243@mails.ucas.ac.cn (Y.L.); wangqianqian22@mails.ucas.ac.cn (Q.W.); liubingyu26@mails.ucas.ac.cn (B.L.)
[2] University of Chinese Academy of Sciences, Beijing 101408, China
[3] Satellite Application Center for Ecology and Environment, Ministry of Ecology and Environment, Beijing 100094, China; liush@secmep.cn
[4] Key Laboratory of Satellite Remote Sensing, Ministry of Ecology and Environment, Beijing 100094, China
* Correspondence: gaogm@secmep.cn

Highlights

What are the main findings?

- An observation-dependent adaptive reference spectrum library is constructed based on SCIATRAN radiative transfer simulation, with surface reflectance and solar zenith angle identified as the dominant influencing parameters for GF-5B GMI spectra.
- The joint spectral--radiometric calibration framework effectively reduces spectral offsets, stabilizes radiometric response and improves spectral-shape consistency for the O_2, CO_2-1, and CO_2-2 bands, which is validated by multi-site observations from Dunhuang, Golmud and Railroad Valley (RRV).

What are the implications of the main findings?

- The physically constrained calibration approach mitigates instrument-induced spectral and radiometric drifts during long-term on-orbit operation, improving the quality of GF-5B GMI Level-1 radiance products.
- The transferable framework supports more reliable greenhouse-gas retrievals and provides a practical reference for on-orbit quality evaluation of future space-borne hyperspectral greenhouse-gas monitoring instruments.

Abstract

Accurate spectral and radiometric calibration is essential for reliable greenhouse gas retrieval from satellite hyperspectral observations. However, long-term in-orbit operation may introduce wavelength shifts and radiometric response inconsistencies, particularly within narrow atmospheric absorption bands, reducing the reliability of Level-1 radiance products. This study proposes an observation-dependent adaptive reference spectrum framework for spectral and radiometric calibration of the Greenhouse Gas Monitoring Instrument (GMI) onboard the GaoFen-5B (GF-5B) satellite. The proposed framework integrates the SCIATRAN radiative transfer model with the instrument line shape (ILS) of GMI to generate physically consistent reference spectra under varying observation conditions. Sensitivity analysis was performed to identify dominant parameters affecting simulated radiance spectra, and an adaptive reference spectrum library was constructed by considering surface reflectance, solar zenith angle, aerosol conditions, and geographic characteristics. The generated reference spectra were subsequently used to estimate spectral shifts and correct radiometric response deviations between observed and simulated spectra.

Check for updates

Academic Editor: Jose Moreno

Received: 3 September 2026
Revised: 11 October 2026
Accepted: 18 October 2026
Published: 21 October 2026

Copyright: © 2026 by the authors. Licensee MDPI, Basel, Switzerland. This article is an open access article distributed under the terms and conditions of the Creative Commons Attribution (CC BY) license.

GF-5B GMI observations acquired from September 2021 to December 2024 over Dunhuang, Golmud, and Railroad Valley (RRV) were used for validation. Results demonstrate that the proposed framework effectively reduces spectral offsets, improves radiometric consistency, and enhances spectral agreement for the O_2, CO_2-1, and CO_2-2 bands. The multi-site validation confirms the robustness of the proposed approach under different surface and atmospheric conditions. This study provides a physically constrained and transferable calibration framework for improving the long-term spectral and radiometric consistency of greenhouse gas hyperspectral observations and supporting more reliable atmospheric composition retrievals.

Keywords: GF-5B GMI; radiometric calibration; spectral calibration; adaptive reference spectrum; SCIATRAN; in-orbit performance evaluation

1. Introduction

Global climate change driven by increasing greenhouse gas concentrations has highlighted the urgent need for accurate and continuous monitoring of atmospheric greenhouse gases [1]. Carbon dioxide (CO_2) and methane (CH_4) observations from satellite-based remote sensing platforms have become an important approach for characterizing global carbon sources and sinks due to their wide spatial coverage and long-term observation capability. The retrieval accuracy of greenhouse gas concentrations, however, strongly depends on the quality of satellite Level-1 radiance measurements. Any systematic errors in spectral calibration or radiometric response may introduce uncertainties into absorption feature characterization and subsequently degrade the reliability of greenhouse gas retrieval products.

In recent years, several dedicated greenhouse gas monitoring satellites and instruments have been developed, including the Orbiting Carbon Observatory-2 (OCO-2) [2], the Greenhouse Gases Observing Satellite (GOSAT) [3], and the TROPOspheric Monitoring Instrument (TROPOMI) [4]. These missions have demonstrated the capability of spaceborne spectrometers to provide global greenhouse gas observations. However, maintaining high-quality measurements during long-term in-orbit operation remains challenging. Long-term in-orbit operation may introduce instrument degradation effects, including radiometric response variations and changes in calibration parameters, which can affect the spectral and radiometric consistency of satellite observations [5]. For high-resolution spectrometers, wavelength calibration errors and variations in the instrument line shape (ILS) may further influence the matching between measured spectra and theoretical atmospheric absorption features, leading to uncertainties in trace gas retrievals [6–8]. These effects are particularly important for greenhouse gas monitoring missions, where small spectral or radiometric deviations within narrow absorption bands may affect the accuracy of retrieved gas concentrations.

In-orbit calibration and quality assessment methods have therefore received increasing attention. Traditional calibration approaches mainly rely on pre-launch laboratory measurements and ground calibration campaigns, which can provide accurate instrument characterization but cannot fully represent long-term variations under actual space conditions. Solar Fraunhofer line-based methods have been widely used for monitoring spectral wavelength stability because solar absorption features provide stable spectral references. However, these approaches mainly focus on spectral wavelength shifts and cannot directly correct radiometric response inconsistencies [9]. In addition, empirical correction meth-

ods based on statistical relationships are computationally efficient but often lack physical constraints, making their applicability limited under different observation conditions.

The Greenhouse Gas Monitoring Instrument (GMI) [10–12] onboard the GaoFen-5B (GF-5B) satellite is a hyperspectral remote sensing payload designed for atmospheric greenhouse gas monitoring. Based on Spatial Heterodyne Spectroscopy (SHS) technology [13], GMI provides high-resolution radiance measurements covering the major O_2 and CO_2 absorption bands. The instrument includes the O_2 absorption band, weak CO_2 absorption band (CO_2-1), and strong CO_2 absorption band (CO_2-2), which are essential for greenhouse gas retrieval. However, long-term in-orbit observations may introduce spectral and radiometric inconsistencies among different channels, affecting the reliability of GMI Level-1 radiance products [14]. Therefore, a physically consistent evaluation and improvement framework is required to characterize and correct these quality degradation effects.

Recently, physics-based reference spectrum approaches have been increasingly applied for satellite spectral and radiometric performance evaluation by comparing measured observations with simulated spectra. Radiative transfer models (RTMs), such as SCIATRAN and MODTRAN, can simulate atmospheric radiance under specified observation geometries, surface reflectance conditions, and atmospheric states, providing a physically consistent baseline for instrument calibration and validation [15,16]. However, most existing approaches rely on predefined reference spectra or limited observation scenarios, which may not fully capture variations caused by surface reflectance, solar zenith angle, and atmospheric conditions. Therefore, constructing adaptive reference spectra that account for observation-dependent parameters is important for reliable long-term instrument quality assessment and calibration.

In this study, a physics-based spectral and radiometric quality improvement framework is proposed for GF-5B GMI observations. The main objectives are to establish an adaptive reference spectrum library, quantify spectral and radiometric inconsistencies, and improve the in-orbit data quality of GMI. The major contributions of this study are summarized as follows:

1. A SCIATRAN-based adaptive reference spectrum library is constructed by considering observation-dependent parameters, including surface reflectance, solar zenith angle, aerosol conditions, and geographic characteristics. Sensitivity analysis is performed to identify dominant parameters affecting simulated radiance spectra, enabling efficient generation of physically consistent reference spectra.
2. A joint spectral and radiometric quality improvement strategy is developed. Spectral recalibration is performed by identifying stable atmospheric absorption features and correcting wavelength-dependent spectral offsets. Radiometric calibration is further applied using global and wavelength-dependent correction factors to compensate systematic response deviations.
3. The proposed framework is evaluated using GF-5B GMI observations acquired from September 2021 to December 2024 over three representative sites, including Dunhuang, Golmud, and Railroad Valley (RRV). The effectiveness of the method is assessed using spectral offset, radiometric response coefficient, and spectral shape consistency indicators, demonstrating the applicability of the proposed approach under different observation conditions.

This study provides a physically constrained and transferable solution for improving the spectral and radiometric quality of GF-5B GMI observations and supports more reliable greenhouse gas retrieval and long-term carbon monitoring applications.

2. Materials and Methods

2.1. GF-5B GMI Data and Calibration Sites

The Greenhouse Gas Monitoring Instrument (GMI) onboard the GaoFen-5B (GF-5B) satellite was developed by the Anhui Institute of Optics and Fine Mechanics, Hefei Institutes of Physical Science, Chinese Academy of Sciences (Hefei, China) [17]. As a hyperspectral remote sensing payload designed to monitor atmospheric greenhouse gases, GMI employs Spatial Heterodyne Spectroscopy (SHS) technology to acquire high-resolution spectral radiance observations in the near-infrared and shortwave-infrared regions, covering the major absorption bands of atmospheric O_2 and CO_2.

In this study, the Level-1 top-of-atmosphere radiance products of GF-5B GMI were used as the primary observations. Three representative absorption bands were selected, including the O_2 band, weak CO_2 absorption band (CO_2-1), and strong CO_2 absorption band (CO_2-2). These three channels cover different spectral regions and exhibit different responses to atmospheric absorption and instrumental characteristics, providing suitable datasets for validating the proposed radiometric and spectral quality improvement framework.The spectral ranges, spectral resolutions, and signal-to-noise ratios of the three selected GMI channels are summarized in Table 1.

Table 1. Main spectral characteristics of the three GMI channels used in this study.

Channel	Spectral Range (nm)	Spectral Resolution	Signal-to-Noise Ratio (SNR)
O_2	759–769	0.6 cm^{-1}/0.035 nm	300
CO_2-1	1568–1583	0.27 cm^{-1}/0.035 nm	250
CO_2-2	2045–2061	0.27 cm^{-1}/0.11 nm	250

Three representative sites, including Dunhuang [18], Golmud [19], and RRV [20], were selected to evaluate the applicability and robustness of the proposed spectral and radiometric quality improvement framework under different surface and atmospheric conditions. These sites cover typical observation environments for satellite remote sensing calibration, including bright arid desert surfaces, high-altitude dry regions, and internationally recognized calibration sites with relatively homogeneous surface characteristics.

The diversity of these sites provides a comprehensive evaluation of the proposed method under different observation geometries, surface reflectance conditions, and radiometric response levels. The geographic coordinates and main characteristics of the three calibration and validation sites are summarized in Table 2. GF-5B GMI observations acquired from September 2021 to December 2024 were collected for these sites. After cloud screening and quality control procedures, the retained observations were used for adaptive reference spectrum construction, spectral consistency evaluation, and radiometric calibration validation. The temporal distribution and number of retained observations for each calibration site are summarized in Table 3.

Table 2. Information of calibration and validation sites used in this study.

Site	Latitude	Longitude	Main Characteristics
Dunhuang	40.14°N	94.32°E	Bright arid Gobi surface with low vegetation coverage and limited cloud interference
Golmud	36.41°N	94.90°E	High-altitude arid region with clear atmospheric conditions and dry surface characteristics
RRV	38.50°N	115.69°W	International satellite calibration site with a spatially homogeneous bright desert surface

Table 3. Number of retained GF-5B GMI observations after quality screening at each calibration site.

Site	September 2021–December 2022	January–December 2023	January–December 2024	Total
Dunhuang	17	22	20	59
Golmud	10	7	15	32
RRV	24	17	10	51
Total	51	46	45	142

2.2. Data Preprocessing

To establish a reliable correspondence between measured GMI radiance and simulated reference spectra, several preprocessing procedures were applied to remove unsuitable observations and ensure consistency between satellite measurements and radiative transfer simulations.

1. **Spatial range selection**

Based on the locations of the calibration and validation sites, GMI observations were first extracted within predefined spatial windows. For each site, a 0.5° × 0.5° square region centered on the corresponding geographic coordinate was established, and only observations located within these regions were retained. This spatial constraint ensured that the selected observations represented consistent surface characteristics and observation conditions for subsequent radiometric and spectral calibration.

2. **Radiance Calculation and Spectral Quality Control**

The L1 product of the GF5B satellite provides DN values and radiation calibration coefficients for each channel. Since the DN value itself has no physical meaning, it must be converted to radiance spectra using the radiation calibration coefficient (CaliCoeff) [11], as shown in the following formula:

$$\text{Radiance} = \text{DN} \times \text{CaliCoeff}(:,1) + \text{CaliCoeff}(:,2) \quad (1)$$

The radiance unit in the GMI L1 product is inconsistent with the output unit of the radiative transfer model, so a unit conversion is required, as shown below:

$$L_{\text{W}} = L_{\text{GMI}} \times \frac{10^5}{\lambda^2} \quad (2)$$

where L_W is the radiance spectrum in units of W/(m^2·sr·nm) from the radiative transfer model, L_{GMI} is the radiance spectrum in units of W/(cm^2·sr·cm^{-1}) from GMI, and λ is the wavelength in nm.

After radiometric conversion, spectral quality control was performed for each absorption band. Since the quality of different GMI channels may vary due to instrument response characteristics and data transmission conditions, invalid spectral measurements were removed independently for each channel. Observations containing zero or negative radiance values, missing spectral samples, or abnormal spectral responses within the corresponding wavelength range were excluded. The remaining valid spectra were retained for subsequent reference spectrum matching and calibration analysis.

3. **Data Screening**

To provide reliable surface and atmospheric parameters for radiative transfer simulations, additional correction and screening procedures were applied to the retained GMI observations. MODIS products, including the cloud products (MOD06/MYD06), surface reflectance product (MOD09GA), and BRDF/albedo model parameters (MCD43A1), were

used in this study. These products are provided by NASA through its Earth Observing System Data and Information System (EOSDIS) and distributed via the corresponding Distributed Active Archive Centers (DAACs) [21–23].

To provide reliable surface and atmospheric parameters for radiative transfer simulations, additional correction and screening procedures were applied to the retained GMI observations. Cloud-contaminated observations were first removed using the MODIS cloud products (MOD06/MYD06) [21]. The cloud mask product provides cloud identification information based on multispectral threshold methods and physical inversion algorithms. Only observations under clear-sky conditions were retained to minimize the influence of cloud contamination on the consistency between measured GMI spectra and simulated reference spectra.

Since the calibration sites cannot be considered ideal Lambertian surfaces, the bidirectional reflectance effect was considered in this study. The MODIS surface reflectance product (MOD09GA) combined with the MCD43A1 BRDF/albedo model parameters was used to correct the surface reflectance to the corresponding observation geometry [22,23]. Specifically, the Ross–Li kernel-driven BRDF model was employed to account for the directional reflectance effects by considering isotropic, volumetric scattering, and geometric-optical scattering components. The BRDF correction factors were calculated using the MCD43A1 model parameters and applied to the MOD09GA surface reflectance to obtain geometrically normalized surface reflectance. The BRDF-corrected MODIS reflectance values were then mapped to the corresponding GMI channels. Specifically, the average reflectance of MODIS band 1 (0.620–0.670 μm) and band 2 (0.841–0.876 μm) was used to represent the surface reflectance of the O_2 channel, while MODIS band 6 (1.628–1.652 μm) and band 7 (2.105–2.155 μm) were used to approximate the surface reflectance of the CO_2-1 and CO_2-2 channels, respectively. The corrected surface reflectance was subsequently used as an input parameter for radiative transfer simulations.

Aerosol effects were further considered using the MERRA-2 reanalysis aerosol product (M2T1NXAER), produced by NASA's Global Modeling and Assimilation Office (GMAO) and distributed by the NASA Goddard Earth Sciences Data and Information Services Center (GES DISC) [24,25], which provides aerosol optical depth (AOD) at 550 nm and the Ångström exponent.

$$AOD(\lambda) = AOD_{550} \times \left(\frac{\lambda}{550}\right)^{-\alpha} \quad (3)$$

where AOD_{550} represents the aerosol optical depth at 550 nm, λ is the target wavelength, and α is the Ångström exponent. Observations with AOD values greater than 0.3 [10] were excluded to reduce aerosol-induced uncertainties in radiative transfer simulations and ensure reliable reference spectrum generation.

3. Physics-Based Adaptive Reference Spectrum Construction

3.1. SCIATRAN Forward Simulation

To establish reliable reference spectra for radiometric and spectral calibration of GMI observations, a physics-based reference spectrum library was constructed using the SCIATRAN radiative transfer model (version 4.6; Institute of Environmental Physics, University of Bremen, Bremen, Germany) [15,26]. The model considers major factors affecting satellite-observed radiance, including atmospheric absorption, aerosol scattering, surface reflectance, and observation geometry. Under specified atmospheric and surface conditions, SCIATRAN was used to simulate high-resolution radiance spectra at the satellite entrance aperture. The simulated spectra were subsequently convolved with the ILS of GMI to generate reference spectra with comparable spectral characteristics to the measured observations. Compared with conventional spectral recalibration approaches, such as solar

Fraunhofer line-based [27] and cross-correlation methods [28], the proposed approach uses SCIATRAN-simulated atmospheric absorption features as wavelength references. Solar Fraunhofer lines provide stable spectral references, while cross-correlation methods can efficiently estimate spectral shifts through spectral similarity matching. The advantage of the proposed approach lies in the use of observation-dependent reference spectra that account for atmospheric absorption, surface reflectance, observation geometry, and the instrument line shape (ILS), making it suitable for the O_2 and CO_2 absorption bands of GMI. However, its accuracy depends on the reliability of the radiative transfer simulations and input parameters, and the reference spectrum generation requires additional computational effort.

The main configuration parameters used in the SCIATRAN forward simulations are summarized in Table 4. In this study, the spherical atmospheric scattering mode was selected to account for the effects of atmospheric geometry, and the discrete ordinate method (DOM) [29] was applied for radiative transfer calculations. The line-by-line (LBL) absorption calculation scheme was adopted to accurately characterize the absorption features of greenhouse gases. The extraterrestrial solar irradiance spectrum, trace gas settings, and spectral simulation ranges were configured according to the characteristics of the GMI absorption bands.

Table 4. Main configurations of the SCIATRAN radiative transfer model.

Parameter	Setting
RTM Mode	Int
RTM_TYPE	Spher_scat
RTM_CORE	DOM_S
Extra-terrestrial solar flux	Solspec_modtran37.dat
Trace gas selection	CO_2
Line absorber treatment	LBL
Do convolution	f
Spectral segment info	Band1: 759–769 nm/0.001 nm Band2: 1568–1583 nm/0.001 nm Band3: 2045–2061 nm/0.001 nm

Based on the above SCIATRAN configurations, high-resolution radiance spectra were simulated at a spectral resolution of 0.001 nm for the three GMI absorption bands. However, the simulated spectra cannot be directly compared with the GMI observations because the spectral response of the instrument causes spectral broadening and smoothing effects. Therefore, the ILS was applied to convolve the simulated spectra and reproduce the spectral response characteristics of the GMI sensor. The ILS describes the instrument's response characteristics to different wavelengths of light, i.e., how the actual signal measured by the instrument is distributed across different wavelengths when the instrument receives light at a single wavelength. Convolution with the ILS is required to correct for instrument effects before comparing the observed spectra [12]. The convolution formula is as follows:

$$I_0(\lambda) = \frac{\int_{\lambda_1}^{\lambda_2} I_{h0}(\lambda')S(\lambda - \lambda')d\lambda'}{\int_{\lambda_1}^{\lambda_2} S(\lambda')d\lambda'} \quad (4)$$

where $I_{h0}(\lambda')$ is the high-resolution radiance spectrum output by the model, λ' is the wavelength of the high-resolution spectrum, λ is the instrument wavelength, $S(\lambda)$ is the instrument line shape function defined at wavelength λ, and $I_0(\lambda)$ is the final reference radiance spectrum calculated.

The ILS-convolved reference spectra preserve the atmospheric absorption characteristics simulated by SCIATRAN while incorporating the spectral response characteristics of the GMI instrument, providing a consistent spectral basis for subsequent calibration.

3.2. Sensitivity Analysis and Parameter Selection

To determine the key parameters affecting the reference spectra and optimize the computational efficiency of the reference spectrum library, a sensitivity analysis was performed based on a one-at-a-time (OAT) strategy [30,31]. Seven input parameters were considered, including solar irradiance model, atmospheric model, aerosol optical depth (AOD), CO_2 concentration, surface reflectance, solar zenith angle (SZA), and geographic location. During the sensitivity analysis, only one parameter was changed each time, while all other parameters were fixed to the reference condition. The parameter ranges were selected to represent typical observation scenarios of GMI, including different surface properties, atmospheric conditions, observation geometries, and instrument simulation settings. The detailed parameter configurations are summarized in Table 5.

Table 5. Parameter settings for sensitivity analysis.

Parameter Name	Setting
Solar Irradiance Model	LOWTRAN, MODTRAN, THKUR
Atmospheric Model	US Standard, Midlatitude Summer, Custom
Aerosol Optical Depth	0.1, 0.2, 0.3, 0.4, 0.5
CO_2 Concentration	380 ppm, 400 ppm, 401 ppm, 420 ppm
Surface Reflectance	0.1, 0.2, 0.3, 0.4, 0.5, 0.6, 0.7, 0.8, 0.9
Solar Zenith Angle	10°, 20°, 30°, 40°, 50°, 60°
Geographic Location	Dunhuang, Golmud, RRV

To quantitatively evaluate the influence of different simulation parameters on the reference spectra, the relative radiance sensitivity (RRS) was introduced as a quantitative sensitivity metric. Since the absolute radiance levels vary among different spectral bands, the normalized relative radiance difference was used instead of the absolute radiance difference to enable a consistent comparison among different channels. The RRS is defined as:

$$RRS_p = \max_i \left[\frac{1}{N} \sum_{k=1}^{N} \frac{|L_i(\lambda_k) - L_0(\lambda_k)|}{|L_0(\lambda_k)|} \right] \quad (5)$$

where RRS_p represents the relative radiance sensitivity of parameter p, $L_i(\lambda_k)$ denotes the simulated radiance at wavelength λ_k under the ith parameter condition, $L_0(\lambda_k)$ represents the radiance spectrum under the reference condition, and N is the number of matched spectral sampling points. A larger RRS value indicates a stronger sensitivity of the simulated reference spectrum to the corresponding parameter.

3.3. Adaptive Reference Spectrum Generation

Based on the identified sensitive parameters, an adaptive reference spectrum library generation strategy was developed to generate reference radiance spectra that closely match the actual GMI observation conditions. Although a discrete reference spectrum library can cover representative observation scenarios, the simulated conditions may not exactly correspond to the measured satellite observations. Therefore, an adaptive interpolation strategy was introduced to achieve continuous matching within the sensitive parameter space.

The reference spectrum library was initially constructed using multiple candidate parameters, and the dominant parameters for adaptive interpolation were subsequently

determined according to the sensitivity analysis results. To maintain a general formulation, the two selected sensitive parameters are denoted as p_1 and p_2, respectively. In this study, p_1 and p_2 correspond to surface reflectance and solar zenith angle, respectively.

The parameter grids are defined as:

$$\{p_{1,1}, p_{1,2}, \cdots, p_{1,m}\} \tag{6}$$

and

$$\{p_{2,1}, p_{2,2}, \cdots, p_{2,n}\} \tag{7}$$

corresponding to the pre-calculated discrete reference radiance spectra:

$$L(\lambda; p_{1,i}, p_{2,j}) \tag{8}$$

where λ represents the wavelength. According to the sensitivity analysis results, surface reflectance and solar zenith angle were selected as the two dominant parameters for adaptive interpolation, while other low-sensitivity parameters were fixed or simplified during the interpolation process.

For any satellite observed condition $(p_{1,obs}, p_{2,obs})$, where $p_{1,obs}$ and $p_{2,obs}$ represent the surface reflectance and solar zenith angle under the actual observation conditions, respectively, with $p_{1,obs}$ obtained from the BRDF-corrected MODIS surface reflectance data and $p_{2,obs}$ obtained from the GMI Level-1 geolocation data, the nearest upper and lower adjacent values in the parameter space are selected as:

$$p_{1,i} \leq p_{1,obs} \leq p_{1,i+1} \tag{9}$$

and

$$p_{2,j} \leq p_{2,obs} \leq p_{2,j+1} \tag{10}$$

The four adjacent reference spectra are then determined as:

$$L(\lambda; p_{1,i}, p_{2,j}), \tag{11}$$

$$L(\lambda; p_{1,i}, p_{2,j+1}), \tag{12}$$

$$L(\lambda; p_{1,i+1}, p_{2,j}), \tag{13}$$

and

$$L(\lambda; p_{1,i+1}, p_{2,j+1}). \tag{14}$$

Based on these adjacent reference spectra, a distance-based weighted interpolation method is applied to construct the adaptive reference radiance spectrum:

$$L_{ref}(\lambda) = \sum_{i=1}^{2} \sum_{j=1}^{2} w_{ij} L(\lambda; p_{1,i}, p_{2,j}) \tag{15}$$

where the weight coefficients w_{ij} are determined according to the distance between the observed conditions and the predefined parameter nodes:

$$w_{ij} = \frac{1}{(|p_{1,i} - p_{1,obs}| + \varepsilon)(|p_{2,j} - p_{2,obs}| + \varepsilon)} \tag{16}$$

where ε is a small positive constant introduced to avoid singularities when the observed condition is exactly equal to one of the predefined parameter nodes. The weights are further normalized to satisfy:

$$\sum_{i=1}^{2}\sum_{j=1}^{2} w_{ij} = 1 \tag{17}$$

This adaptive weighting strategy enables a continuous representation of the two dominant sensitive parameters, i.e., surface reflectance and solar zenith angle, effectively reducing the mismatch between discrete reference spectra and actual satellite observation conditions. It minimizes the influence of observation geometry and surface variability on the spectral evaluation results and provides a unified and stable physical reference baseline for long-term and multi-scenario radiometric and spectral performance analysis.

To further verify the effectiveness of the adaptive reference spectrum generation strategy, the consistency between the interpolated reference spectra and directly simulated SCIATRAN spectra was quantitatively evaluated under different observation conditions.

To evaluate the interpolation accuracy of the adaptive reference spectrum library, nine independent SCIATRAN simulation scenarios were selected across the three GMI spectral bands, covering different combinations of surface reflectance (0.15, 0.45, and 0.75) and solar zenith angle (15°, 35°, and 55°). These validation scenarios were not included in the reference spectrum library. For each scenario, the adaptive reference spectrum generated through interpolation was compared with the corresponding spectrum directly simulated by SCIATRAN. The agreement was quantitatively evaluated using the root mean square error (RMSE), normalized root mean square error (NRMSE), and coefficient of determination (R^2).

The validation results are presented in Table 6. Across the nine scenarios, the NRMSE ranged from 1.99% to 5.59%, while the R^2 values ranged from 0.9479 to 0.9987. For the O_2 band, the NRMSE remained between 3.81% and 4.04%, with R^2 values exceeding 0.996. The CO_2-1 and CO_2-2 bands also showed good agreement between the interpolated and directly simulated spectra, with NRMSE values below 5.60% and R^2 values above 0.94. These results indicate that the adaptive reference spectrum library can reproduce directly simulated SCIATRAN spectra with good accuracy under the tested observation conditions, supporting its applicability to observation-dependent reference spectrum generation for GF-5B GMI.

Table 6. Accuracy assessment of adaptive reference spectra against directly simulated SCIATRAN spectra under nine independent validation scenarios.

Band	Reflectance	SZA (°)	RMSE	NRMSE (%)	R^2
O_2	0.15	15	1.3383	3.8058	0.9963
O_2	0.75	35	5.4305	3.9760	0.9965
O_2	0.45	55	2.1897	4.0354	0.9967
CO_2-1	0.45	15	0.9151	2.8555	0.9727
CO_2-1	0.15	35	0.2468	2.7273	0.9770
CO_2-1	0.75	55	1.4128	4.5474	0.9479
CO_2-2	0.75	15	0.6868	4.5957	0.9913
CO_2-2	0.45	35	0.4137	5.5895	0.9880
CO_2-2	0.15	55	0.0322	1.9898	0.9987

3.4. Joint Spectral and Radiometric Quality Improvement

The adaptive reference spectrum library constructed in Section 3 provides physically consistent reference radiance spectra under different observation conditions. Based on these reference spectra, a joint spectral and radiometric calibration method was developed to improve the in-orbit quality of GMI observations. The proposed framework includes spectral recalibration to correct wavelength-dependent deviations and radiometric calibration to compensate systematic response differences between the measured and reference spectra. The overall process of the method is shown in Figure 1.

To evaluate the effectiveness of the proposed spectral and radiometric quality improvement framework, three types of evaluation indicators were adopted, including absolute spectral offset, radiometric response coefficient (k), and spectral consistency metrics. These indicators were selected to characterize different aspects of hyperspectral observation quality. Specifically, the absolute spectral offset was used to evaluate wavelength localization accuracy and spectral calibration performance, the radiometric response coefficient (k) was used to quantify the consistency between observed and reference radiance and assess radiometric response stability, and the spectral consistency metrics were used to evaluate the agreement of spectral shape between observed and reference spectra. Together, these indicators provide complementary assessments of spectral accuracy, radiometric consistency, and spectral fidelity, which are the key aspects considered in this study for evaluating the on-orbit quality improvement of GF-5B GMI observations.

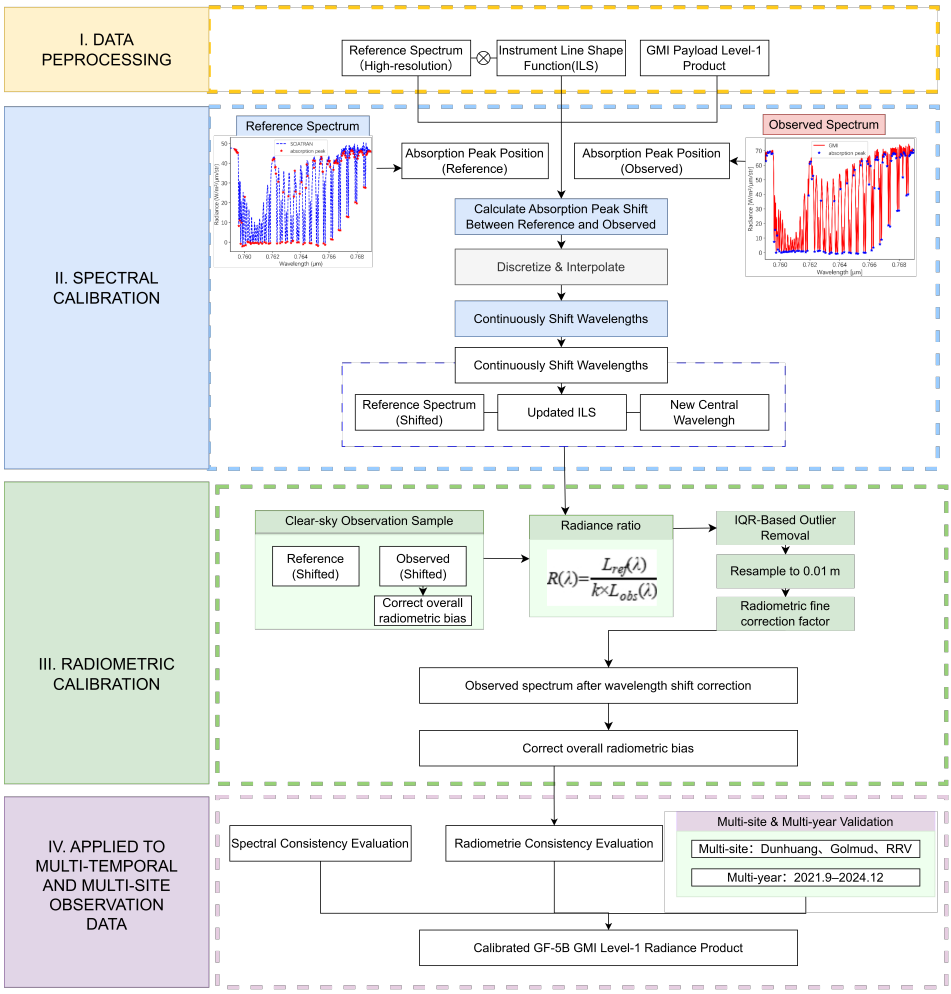


Figure 1. Radiation spectrum quality improvement process flowchart.

3.4.1. Spectral Recalibration

The spectral accuracy of satellite-borne hyperspectral instruments may be affected by multiple factors during long-term in-orbit operation, including detector aging, thermal environment variation, and optical system instability. These factors may introduce wavelength-dependent spectral shifts between the nominal and actual spectral response functions, resulting in spectral mismatch between the measured observations and the reference spectra. To reduce the influence of observation condition differences on spectral shift estimation, the adaptive reference spectra generated in Section 3.3 were adopted as the physical spectral reference. Unlike fixed reference spectra, the adaptive reference

spectra were generated according to the corresponding observation geometry and surface conditions, providing a more accurate spectral reference for each GMI observation.

The spectral shift was estimated by comparing the absorption feature positions between the observed GMI spectra and the corresponding reference spectra. Since the O_2 A-band, CO_2-1 band, and CO_2-2 band contain relatively stable atmospheric absorption features, these absorption structures can serve as reliable wavelength references for spectral recalibration. The positions of these absorption features are primarily determined by molecular absorption characteristics and are less affected by variations in surface reflectance and observation conditions, making them suitable for detecting wavelength-dependent spectral shifts.

The absorption peak positions of both the reference spectra and the observed spectra were identified based on the first-order derivative-based peak detection method. Specifically, the zero-crossing points of the first-order derivative were initially detected, and local minimum constraints were further applied to eliminate false peaks caused by spectral fluctuations and noise. The local minimum constraint requires that the detected absorption feature corresponds to the minimum radiance value within a predefined wavelength window around the candidate peak.An example of absorption peak identification in the observed and reference spectra for the O_2 channel is shown in Figure 2.

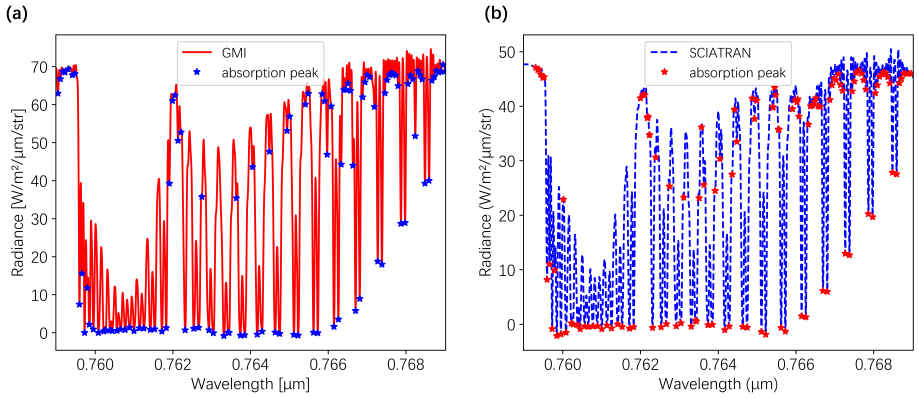


Figure 2. Absorption peak identification between the observed and reference spectra in the O_2 channel (6 October 2022). (**a**) Observed Spectrum Absorption Peak Identification Results; (**b**) Reference Spectrum Absorption Peak Identification Results

The constraint is expressed as:

$$L(\lambda_i) = \min\{L(\lambda_{i-w}), L(\lambda_{i-w+1}), \cdots, L(\lambda_{i+w})\} \tag{18}$$

where w represents the half-width of the searching window. Based on multiple tests using representative GMI spectra, w was set to 20 in this study. This condition ensures that the identified absorption peaks have a pronounced concave shape, consistent with the physical characteristics of absorption features. For each observation, the adaptive reference spectrum corresponding to the measured conditions was first generated, and the wavelength shift was then determined by matching the absorption features between the measured and reference spectra. The wavelength shift of each absorption feature was calculated as:

$$\Delta\lambda_i = \lambda_{o,i} - \lambda_{r,i} \tag{19}$$

where $\lambda_{o,i}$ and $\lambda_{r,i}$ represent the wavelength positions of the i-th absorption feature identified from the observed and reference spectra, respectively, and $\Delta\lambda_i$ represents the corresponding wavelength shift.

By matching the absorption peak positions between the reference and observed spectra, wavelength shift values can be obtained at several characteristic wavelengths. However, these discrete shift values cannot represent the continuous wavelength-dependent variation within the entire spectral channel. Therefore, linear interpolation was applied to extend the discrete wavelength shifts into a continuous wavelength shift function across the full spectral range.

Using the continuous wavelength shift results, the wavelength for each data point in the GMI observed spectrum is corrected. The calculation formula is:

$$\lambda_{new,i} = \lambda_{o,i} - \Delta\lambda_i \tag{20}$$

where $\lambda_{o,i}$ is the original observed spectrum's center wavelength, $\Delta\lambda_i$ is the wavelength shift, and $\lambda_{new,i}$ is the corrected center wavelength.

The new center wavelengths and observed radiance constitute the GMI observed spectrum after spectral recalibration. Using the new center wavelengths, the high-resolution reference spectrum generated by the SCIATRAN radiative transfer model is convolved with the instrument line shape function, yielding the recalibrated reference spectrum. The convolution formula is as follows:

$$I_0(\lambda_{new}) = \frac{\int_{\lambda_1}^{\lambda_2} I_{h0}(\lambda')S(\lambda_{new} - \lambda')d\lambda'}{\int_{\lambda_1}^{\lambda_2} S(\lambda')d\lambda'} \tag{21}$$

where $I_{h0}(\lambda')$ is the high-resolution radiance spectrum output from the model, λ' is the wavelength of the high-resolution spectrum, λ_{new} is the new wavelength, and $S(\lambda)$ is the instrument line shape function defined at λ, and $I_0(\lambda_{new})$ is the final recalibrated reference spectrum.

3.4.2. Radiometric Calibration

The adaptive reference spectra generated in Section 3.3 provide physically consistent radiance baselines under corresponding observation conditions. Based on these reference spectra, a two-step radiometric calibration method was developed to correct the systematic response deviations and wavelength-dependent radiometric inconsistencies in the GMI observations.

The observed radiance spectrum and reference spectrum should theoretically exhibit a linear relationship under identical observation conditions. However, due to detector response variation, instrument aging, and calibration uncertainty during long-term in-orbit operation, systematic radiometric biases may exist between the observed and reference spectra. Therefore, a least-squares fitting method was first applied to estimate the overall radiometric response coefficient k, which was used to compensate for the global radiometric response deviation:

$$k = \frac{\sum_\lambda L_{ref}(\lambda)L_{obs}(\lambda)}{\sum_\lambda L_{obs}^2(\lambda)} \tag{22}$$

where $L_{ref}(\lambda)$ and $L_{obs}(\lambda)$ denote the reference and observed radiance at wavelength λ, respectively. The coefficient k represents the overall radiometric response difference between the observed spectrum and the reference spectrum.

After removing the global radiometric response bias, residual wavelength-dependent response differences may still exist due to the nonuniform spectral response characteristics of the instrument. Therefore, a fine radiometric calibration procedure was further developed to correct these residual deviations. The wavelength-dependent radiometric deviation was characterized by calculating the radiance ratio between the reference spectrum and the globally corrected observed spectrum:

$$R(\lambda) = \frac{L_{ref}(\lambda)}{k \times L_{obs}(\lambda)} \tag{23}$$

where $R(\lambda)$ represents the wavelength-dependent radiometric response ratio after global correction.

Due to the presence of saturated absorption regions and low signal levels, especially within the O_2 absorption band, small radiance values may introduce abnormal fluctuations in the calculated radiance ratios. Therefore, the interquartile range (IQR) method was applied to remove statistical outliers. The first quartile Q_1 and third quartile Q_3 were calculated, and the interquartile range was defined as:

$$IQR = Q_3 - Q_1 \tag{24}$$

The valid range was determined as:

$$[Q_1 - 1.5 \times IQR,\ Q_3 + 1.5 \times IQR] \tag{25}$$

Values outside this range were removed to ensure the physical reliability and stability of the correction factor.

After outlier removal, the remaining radiance ratio data were resampled with a wavelength interval of 0.01 nm. The mean value within each wavelength interval was calculated to generate a smooth wavelength-dependent radiometric correction factor:

$$k(\lambda) = mean(R(\lambda)) \tag{26}$$

where $k(\lambda)$ represents the fine radiometric calibration factor, which characterizes the residual wavelength-dependent response differences after the global radiometric correction.

The obtained fine calibration factor mainly represents the intrinsic wavelength-dependent response characteristics of each GMI channel after removing the global radiometric response deviation. Since the systematic response deviations caused by instrument characteristics are relatively stable within the same channel over a limited operation period, the fine calibration factor derived from representative clear-sky observations can be transferred to other observations acquired by the same channel under comparable observation conditions.

Therefore, representative clear-sky observations from typical calibration regions were selected to construct channel-specific fine radiometric calibration factors. The selection of representative samples followed three criteria: (1) clear-sky conditions with minimized cloud contamination; (2) reliable spectral quality without abnormal radiometric values; and (3) stable observation conditions over typical calibration sites. These criteria were adopted to minimize uncertainties caused by atmospheric variability, surface heterogeneity, and observation anomalies. Considering the long-term operation of GF-5B GMI, the acquisition time of calibration observations was also considered during the sample selection process. Since the O_2, WCO_2, and SCO_2 absorption bands have different spectral characteristics and observation quality after data screening, the observation acquired at one specific time may not always provide suitable calibration information for all spectral channels. Therefore, representative samples were independently selected for each spectral channel to ensure the reliability of the corresponding fine radiometric calibration factors.Specifically, the fine calibration samples were selected from the Dunhuang, Geermu, and RRV sites. For the Dunhuang site, the selected samples included the O_2 channel observation acquired on 14 September 2023, the WCO_2 channel observation acquired on 26 January 2024, and the SCO_2 channel observation acquired on 6 April 2022. For the Geermu site, the selected samples included the O_2 channel observation acquired on 19 December 2022, the WCO_2 channel

observation acquired on 12 October 2024, and the SCO_2 channel observation acquired on 14 January 2022. For the RRV site, the selected samples included the O_2 channel observation acquired on 17 November 2023, the WCO_2 channel observation acquired on 3 September 2023, and the SCO_2 channel observation acquired on 3 September 2023.

The fine radiometric calibration factors derived from these representative samples were subsequently applied to the corresponding spectral channels of GMI observations. The corrected observations were then used for subsequent radiometric performance analysis.

3.5. Uncertainty Analysis

The proposed calibration framework relies on physics-based reference spectra generated by SCIATRAN simulations, adaptive reference spectrum construction, and representative observations for deriving radiometric calibration factors. Therefore, uncertainties introduced during different stages of the calibration process may affect the final spectral and radiometric calibration results.

In this study, three major uncertainty sources associated with the proposed calibration framework were investigated, including: (1) uncertainties associated with radiative transfer simulations; (2) uncertainties introduced during adaptive reference spectrum generation; and (3) uncertainties associated with the derivation of radiometric calibration factors and scenario variability.

Different evaluation methods were adopted according to the physical characteristics of each uncertainty source. The uncertainty associated with SCIATRAN simulation parameters was quantified through parameter perturbation, while the uncertainties introduced by adaptive reference spectrum generation and calibration factor derivation were evaluated using spectral consistency and statistical variability analysis, respectively.

3.5.1. Uncertainty Associated with SCIATRAN Simulations

The first uncertainty source is associated with the SCIATRAN radiative transfer simulations. Since the reference spectra used in this study were generated based on SCIATRAN, uncertainties in the model input parameters may directly affect the simulated radiance and subsequently influence the accuracy of the reference spectra.

The uncertainty contribution of each input parameter was quantified by comparing the perturbed simulation results with the reference condition:

$$U_i = \frac{|X_i - X_0|}{X_0} \times 100\% \tag{27}$$

where X_0 represents the simulated radiance under the reference condition, and X_i represents the simulated radiance after introducing the corresponding parameter perturbation.

The uncertainty analysis considered the main SCIATRAN input parameters, including the solar irradiance model, atmospheric parameters, surface reflectance, and BRDF model. The atmospheric parameters include aerosol optical depth (AOD), atmospheric temperature and pressure profiles, and greenhouse gas concentrations. These parameters are consistent with those investigated in the sensitivity analysis.

For each parameter, only one variable was perturbed while all other parameters remained unchanged. The uncertainty contributions were then calculated using Equation (27).

The uncertainty introduced by the solar irradiance model was 1.64%, 1.50%, and 0.76% for the O_2, CO_2-1, and CO_2-2 bands, respectively. The combined uncertainty from atmospheric parameters, including AOD, atmospheric profiles, and greenhouse gas concentrations, was 2.24%, 1.13%, and 2.45% for the three bands.

The surface reflectance and BRDF model introduced uncertainties of less than 6% and approximately 1%, respectively. Considering that different uncertainty sources were

independent, the total uncertainty associated with SCIATRAN simulations was calculated using the root-sum-square (RSS) method:

$$U_{SCIATRAN} = \sqrt{U_{solar}^2 + U_{atmosphere}^2 + U_{surface}^2 + U_{BRDF}^2} \quad (28)$$

where U_{solar}, $U_{atmosphere}$, $U_{surface}$, and U_{BRDF} represent the uncertainty contributions from the solar irradiance model, atmospheric parameters, surface reflectance, and BRDF model, respectively.

The total uncertainties associated with SCIATRAN simulations were 6.69%, 6.37%, and 6.60% for the O_2, CO_2-1, and CO_2-2 bands, respectively.

Among all uncertainty sources, surface reflectance contributed the largest uncertainty due to the strong dependence of solar-reflective radiance on surface reflection characteristics. The atmospheric parameters and solar irradiance model introduced relatively smaller uncertainties, indicating that the SCIATRAN-based reference spectra maintain good stability under the investigated observation conditions.

3.5.2. Uncertainty Associated with Adaptive Reference Spectrum Generation

The second uncertainty source is related to the adaptive reference spectrum generation. In this study, observation-dependent reference spectra were generated using the adaptive interpolation strategy described in Section 3.3. Although this strategy improves the efficiency of reference spectrum generation, interpolation may introduce uncertainties compared with directly simulated SCIATRAN spectra.

Therefore, the uncertainty introduced by the adaptive reference spectrum generation was evaluated by comparing the interpolated reference spectra with the corresponding directly simulated SCIATRAN spectra under identical observation conditions. The independent validation scenarios, including different surface reflectance and solar zenith angle combinations, were consistent with those described in Section 3.3.

The consistency between adaptive reference spectra and SCIATRAN spectra was quantified using NRMSE and R^2. The average NRMSE values were 3.94%, 3.38%, and 4.06% for the O_2, CO_2-1, and CO_2-2 bands, respectively. The corresponding average R^2 values were 0.9965, 0.9660, and 0.9927.

These results demonstrate that the adaptive reference spectrum generation introduces limited uncertainty and can effectively reproduce the directly simulated SCIATRAN spectra under different observation conditions.

3.5.3. Uncertainty Associated with Calibration Factor Derivation and Scenario Variability

The third uncertainty source is associated with the derivation of fine radiometric calibration factors and the variability among different calibration scenarios. In this study, representative observations from Dunhuang, Geermu, and RRV were selected to derive the fine radiometric calibration factors.

Although these observations were selected under clear-sky conditions with reliable spectral quality, differences in surface characteristics, atmospheric conditions, and observation geometry among different calibration sites may introduce variations in the derived calibration factors.

Therefore, the scenario-induced uncertainty was evaluated by independently deriving calibration factors from different calibration sites and calculating the relative standard deviation (RSD) of the obtained factors:

$$U_{scenario} = \frac{\sigma_k}{\bar{k}} \times 100\% \quad (29)$$

where σ_k represents the standard deviation of calibration factors derived from different scenarios, and $\bar{k}$ represents their mean value.

The obtained scenario-induced uncertainties were 4.51%, 1.05%, and 6.68% for the O_2, CO_2-1, and CO_2-2 bands, respectively.

The CO_2-1 band exhibited the lowest scenario-induced uncertainty, indicating that the derived calibration factors maintained high consistency among different calibration scenarios. In contrast, the O_2 and CO_2-2 bands showed relatively larger variations, which may be related to their higher sensitivity to solar illumination geometry, atmospheric optical path variations, and surface reflectance differences.

Specifically, the O_2 band is more sensitive to solar zenith angle variations, whereas the CO_2-2 band is more affected by surface reflectance and atmospheric radiative transfer conditions due to its stronger absorption characteristics. These variations represent the physical differences among calibration scenarios rather than instability of the proposed calibration method.

4. Results

4.1. Sensitivity Analysis of Reference Spectrum Parameters

The sensitivity analysis results based on the RRS metric are illustrated in Figure 3. The results demonstrate that different input parameters have distinct impacts on the simulated radiance spectra of the three GMI channels. Among all investigated parameters, surface reflectance exhibited the strongest influence on the reference spectra. The RRS values exceeded 150% for all three spectral bands, with the largest variation observed in the CO_2-1 channel. This indicates that the top-of-atmosphere radiance measured by GMI is highly dependent on surface-reflected solar radiation. Therefore, accurate characterization of surface reflectance is essential for generating reliable reference spectra.

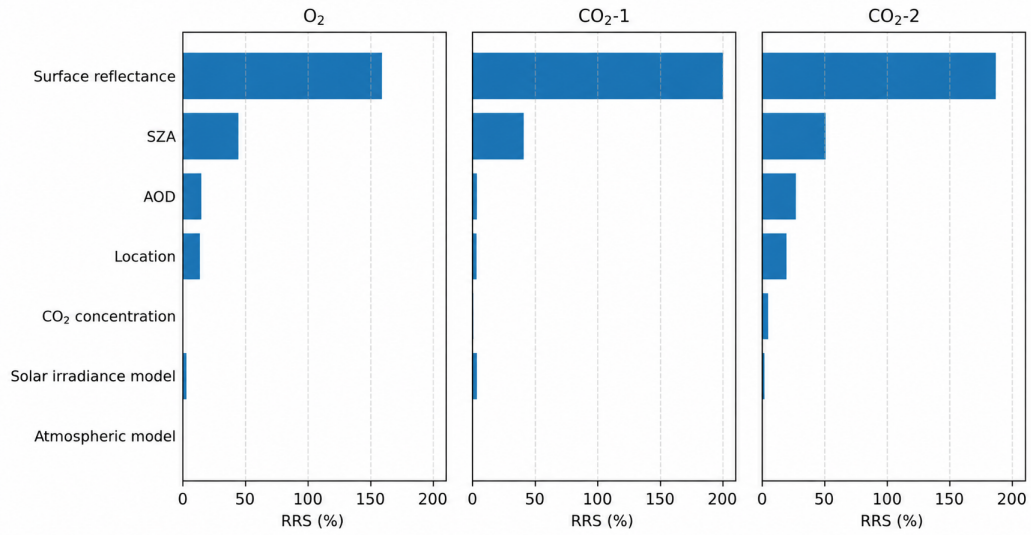


Figure 3. Sensitivity analysis of simulation parameters based on relative radiance variation (RRS) for reference spectrum library construction.

Moderate sensitivity was observed for aerosol optical depth (AOD) and geographic location.The impact of AOD was wavelength-dependent, with a relatively stronger influence on the CO_2-2 channel (RRS = 26.07%) compared with the O_2 and CO_2-1 channels. Geographic location also introduced noticeable spectral variations, particularly in the CO_2-2 band, with an RRS of 18.62%, which can be attributed to differences in surface characteristics and atmospheric background conditions among different calibration sites.

In contrast, CO_2 concentration, solar irradiance model, and atmospheric model showed limited effects on the simulated spectra. The solar irradiance model produced RRS values below 3.1% for all three channels, while the atmospheric model caused negligible variations under the tested conditions. Although CO_2 concentration directly affects gas absorption characteristics, its influence on the overall radiance variation remained relatively small within the investigated concentration range (380–420 ppm). These results indicate that these parameters can be simplified during reference spectrum library construction without significantly reducing spectral simulation accuracy.

Based on the above sensitivity analysis, surface reflectance and SZA were selected as dominant parameters requiring detailed sampling in the reference spectrum library. AOD and geographic location were retained to represent different atmospheric and surface observation scenarios, whereas low-sensitivity parameters were fixed or simplified to improve computational efficiency.

It should be noted that the OAT sensitivity analysis primarily evaluates the individual effects of different parameters and does not explicitly quantify nonlinear interactions among them. In practice, multiple parameters may jointly influence the simulated radiance spectra, particularly surface reflectance and solar zenith angle. In this study, these two dominant parameters were incorporated into the adaptive reference spectrum library through two-dimensional parameter combinations, allowing their combined effects on radiance to be represented. Although higher-order interactions among multiple parameters were not explicitly evaluated, this approach provides a practical balance between physical representation and computational efficiency.

4.2. Spectral Quality Improvement

To evaluate the long-term spectral quality improvement performance of the proposed calibration method, GMI observations acquired over the Dunhuang site from September 2021 to December 2024 were selected for analysis. A series of quality control procedures were applied to exclude observations affected by invalid radiance measurements, excessive aerosol loading, and unsuitable observation conditions. The retained observations were then processed using the proposed adaptive reference spectrum generation and spectral recalibration method.

Since spectral offsets can occur in either positive or negative directions, the sign of the wavelength shift only represents the direction of spectral displacement rather than the magnitude of calibration error. Therefore, the absolute spectral offset $|\Delta\lambda|$ was adopted as the evaluation metric to quantitatively compare the spectral performance before and after calibration. Figure 4 illustrates the temporal evolution of $|\Delta\lambda|$ for the three GMI absorption bands before and after spectral recalibration. The scattered points represent individual GMI observations, and the fitted curves indicate the corresponding long-term variation trends of spectral offsets.

As shown in Figure 4, all three absorption bands exhibit a clear reduction in $|\Delta\lambda|$ after spectral recalibration. Compared with the original observations, the recalibrated results show smaller spectral offset magnitudes and more stable temporal variations, indicating that the proposed method effectively reduces the spectral mismatch between the measured spectra and the adaptive reference spectra.

To quantitatively evaluate the improvement in spectral calibration performance, the statistical comparison of absolute spectral offsets before and after recalibration for the Dunhuang observations is summarized in Table 7. The mean absolute spectral offsets of the O_2, CO_2-1, and CO_2-2 bands decreased from 0.002604 nm, 0.002803 nm, and 0.029378 nm before recalibration to 0.000595 nm, 0.000390 nm, and 0.002359 nm after recalibration, corresponding to reductions of 77.2%, 86.1%, and 92.0%, respectively.

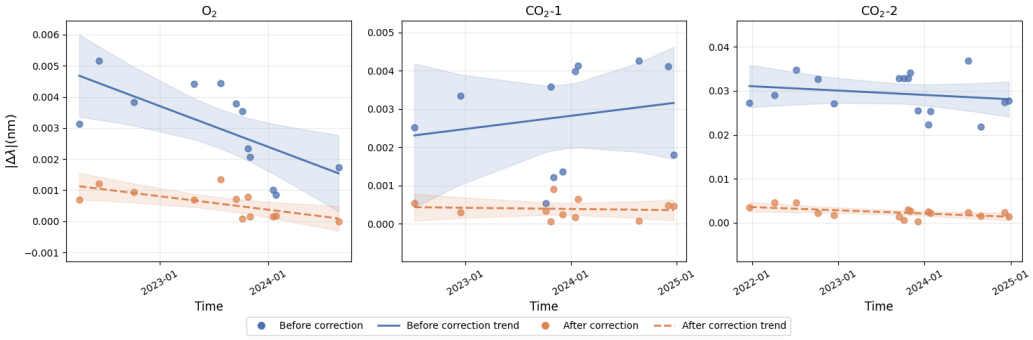


Figure 4. Temporal evolution of absolute spectral offsets before and after spectral recalibration for three GMI absorption bands. The points represent individual observations, and the solid and dashed lines indicate the corresponding long-term variation trends before and after calibration, respectively, and the shaded areas represent the approximate 95% confidence intervals of the fitted trends.

Table 7. Statistical comparison of absolute spectral offsets before and after spectral recalibration at the Dunhuang site.

Band	Samples	$\overline{\lvert\Delta\lambda\rvert}_{before}$ (nm)	$\overline{\lvert\Delta\lambda\rvert}_{after}$ (nm)	Reduction (%)
O_2	14	0.002604	0.000595	77.2
CO_2-1	11	0.002803	0.000390	86.1
CO_2-2	16	0.029378	0.002359	92.0

For the O_2 A-band, the spectral offsets before calibration show relatively large variations during the observation period. After spectral recalibration, the offset magnitude is significantly reduced and remains close to zero, demonstrating improved wavelength alignment and enhanced long-term spectral stability.The CO_2-1 band presents relatively small spectral offsets before calibration, but temporal fluctuations are still observed throughout the monitoring period. After applying the proposed recalibration method, the offset values are further reduced and exhibit a weaker temporal variation, indicating improved spectral consistency for this weak absorption band. The CO_2-2 band exhibits the largest spectral offsets among the three channels before calibration, which is mainly attributed to its strong absorption characteristics and higher sensitivity to spectral response uncertainty. After recalibration, the absolute offset magnitude is substantially reduced, and the temporal variation becomes more stable. These results demonstrate that the proposed adaptive reference spectrum generation and spectral recalibration method can effectively correct channels with larger spectral mismatches.

To further illustrate the spectral recalibration effect, a CO_2-2 spectrum acquired over Dunhuang on 14 December 2022 was selected as an example for comparing the spectra before and after correction. As shown in Figure 5a, noticeable discrepancies exist between the original observed spectrum and the reference spectrum, particularly in the absorption feature regions. These differences indicate that the original GMI spectrum suffers from spectral mismatch caused by wavelength response deviation.

After spectral recalibration, the corrected observed spectrum shows improved agreement with the reference spectrum (Figure 5b). The absorption structures are better aligned, particularly around the major CO_2 absorption features. Quantitatively, the absolute spectral offset decreased from 0.003337 nm before recalibration to 0.000309 nm after recalibration, corresponding to a reduction of approximately 90.7%. This result further confirms that the proposed spectral calibration method can effectively improve the spectral matching accuracy of GMI observations.

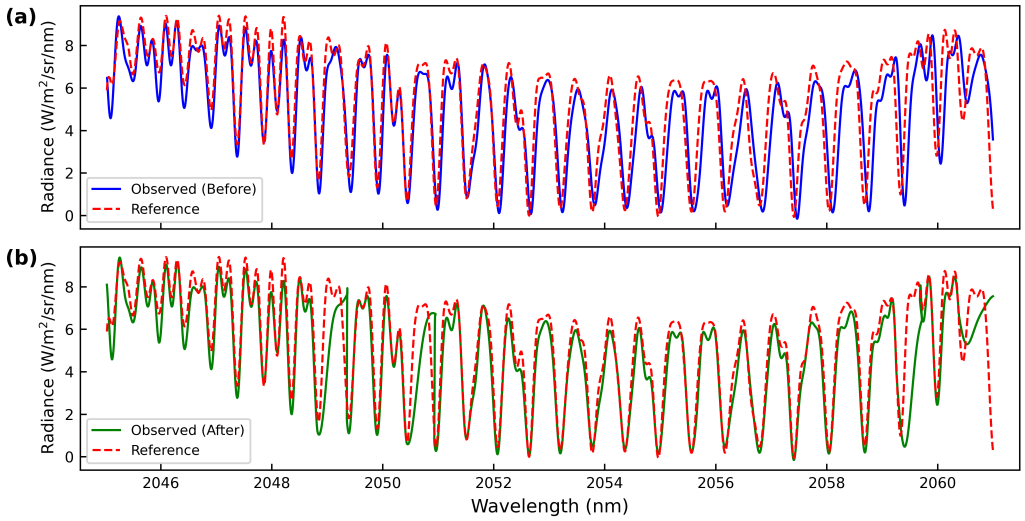


Figure 5. Comparison of CO_2-2 channel spectra before and after spectral recalibration (Dunhuang, 14 December 2022). (**a**) Original observed spectrum and reference spectrum; (**b**) recalibrated observed spectrum and reference spectrum.

4.3. Radiometric Quality Improvement

To evaluate the effectiveness of the proposed radiometric calibration method, GMI observations acquired over the Dunhuang site from September 2021 to December 2024 were selected for validation. After applying quality control procedures, including the removal of observations affected by invalid radiance measurements and unsuitable atmospheric conditions, the retained observations were processed using the proposed adaptive reference spectrum generation and radiometric correction method.

The radiometric response coefficient k, defined in Equation (22), was adopted to evaluate the radiometric response consistency between the observed spectra and the corresponding reference spectra before and after calibration. Ideally, k approaches unity when the observed radiance agrees with the reference radiance, indicating that the systematic radiometric response bias has been effectively corrected. Therefore, the deviation of k from one was used to characterize the radiometric response consistency.

In addition, the coefficient of determination (R^2) between the observed spectra and the reference spectra was used to evaluate the consistency of spectral shape before and after calibration. A higher R^2 value indicates a stronger agreement in spectral variation characteristics between the measured and reference spectra.

Figure 6 presents the temporal evolution of the radiometric response coefficient k before and after calibration for the three GMI absorption bands. The scattered points represent individual GMI observations, and the fitted curves indicate the corresponding long-term variation trends of the radiometric response coefficient.

As shown in Figure 6, the proposed radiometric calibration method improves the temporal stability of the radiometric response coefficient for all three absorption bands. After calibration, the k values become closer to the ideal value of one and exhibit reduced temporal fluctuations, demonstrating improved consistency between the observed radiance spectra and the reference spectra.

The statistical comparison of radiometric response consistency before and after calibration is summarized in Table 8. Specifically, the mean absolute deviation of the radiometric response coefficient from unity ($|k-1|$) was calculated for each absorption band. A smaller $|k-1|$ value indicates better agreement between the observed radiance and the reference radiance.

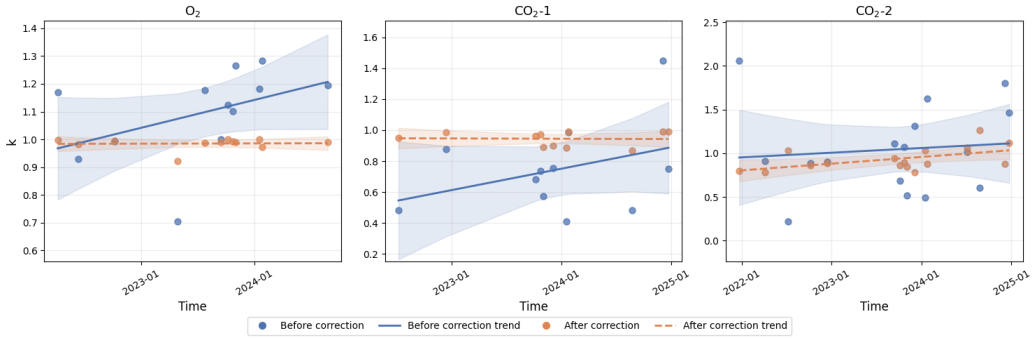


Figure 6. Temporal evolution of the radiometric response coefficient k before and after calibration for three GMI absorption bands. The points represent individual observations, and the solid and dashed lines indicate the corresponding long-term variation trends before and after calibration, respectively, and the shaded areas represent the approximate 95% confidence intervals of the fitted trends.

Table 8. Quantitative comparison of radiometric response consistency before and after calibration at the Dunhuang site.

Band	Samples	$\overline{\lvert k-1\rvert}_{\text{before}}$	$\overline{\lvert k-1\rvert}_{\text{after}}$	Reduction (%)
O_2	14	0.202792	0.006289	96.90
CO_2-1	11	0.337298	0.010009	97.03
CO_2-2	16	0.388861	0.131559	66.17

For the O_2 channel, the k values before calibration exhibit relatively large temporal variations around the ideal value of one, indicating residual radiometric response uncertainties during the observation period. After calibration, the k values become more concentrated around unity. Quantitatively, the mean deviation of k from unity ($|k-1|$) decreased from 0.202792 to 0.006289 (Table 8), confirming the significant improvement in radiometric response consistency.The CO_2-1 channel shows larger deviations of k from unity before calibration, indicating stronger radiometric response inconsistencies. After applying the proposed correction method, the k values are effectively adjusted toward the ideal value of one, and the mean $|k-1|$ decreased from 0.337298 to 0.010009 (Table 8). This result demonstrates that the proposed method effectively compensates for radiometric response biases in the CO_2-1 channel.The CO_2-2 channel exhibits the largest temporal variation in k among the three channels before calibration, reflecting relatively unstable radiometric response characteristics. Although residual variations remain after calibration, the mean $|k-1|$ decreased from 0.388861 to 0.131559 (Table 8), indicating that the proposed calibration method substantially improves the radiometric response consistency of the CO_2-2 channel.

Figure 7 further presents the temporal evolution of R^2 values before and after radiometric calibration for the three GMI absorption bands. The scattered points represent individual spectral comparisons, and the fitted curves describe the long-term variation trends of spectral consistency.

The statistical comparison of R^2 values before and after calibration is summarized in Table 9. The mean R^2 values of the CO_2-1 and CO_2-2 bands increased from 0.645370 and 0.451874 before calibration to 0.865049 and 0.865420 after calibration, respectively, demonstrating a substantial improvement in spectral shape consistency. In contrast, the O_2 band showed relatively limited improvement because its initial spectral consistency was already high. Overall, the results indicate that the proposed radiometric correction method improves the spectral shape consistency between the observed spectra and the reference spectra.

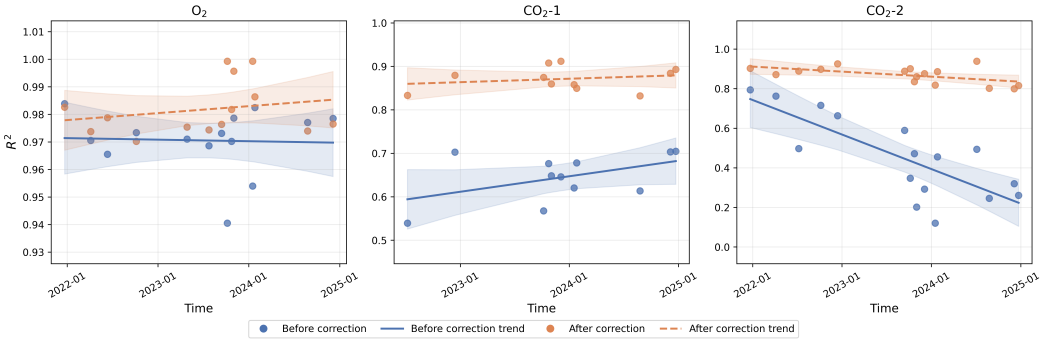


Figure 7. Temporal evolution of R^2 before and after radiometric calibration for three GMI absorption bands. The points represent individual observations, and the solid and dashed lines indicate the corresponding long-term variation trends before and after calibration, respectively, and the shaded areas represent the approximate 95% confidence intervals of the fitted trends.

Table 9. Quantitative comparison of spectral shape consistency before and after radiometric calibration at the Dunhuang site.

Band	Samples	$\overline{R^2}_{\text{before}}$	$\overline{R^2}_{\text{after}}$	Improvement (%)
O_2	14	0.970529	0.981732	1.15
CO_2-1	11	0.645370	0.865049	34.04
CO_2-2	16	0.451874	0.865420	91.52

After the statistical evaluation, an O_2-channel observation acquired over Dunhuang on 6 April 2022 was selected as an illustrative example to visually demonstrate the spectral changes before and after radiometric calibration (Figure 8). Before calibration, obvious discrepancies can be observed between the original observed spectrum and the reference spectrum (Figure 8a). Although the absorption feature positions are generally consistent, indicating that the spectral alignment is reliable, noticeable differences remain in the radiance magnitude, particularly in the high-radiance continuum regions and several absorption feature regions. These discrepancies mainly originate from the radiometric response difference between the observed spectrum and the reference spectrum.

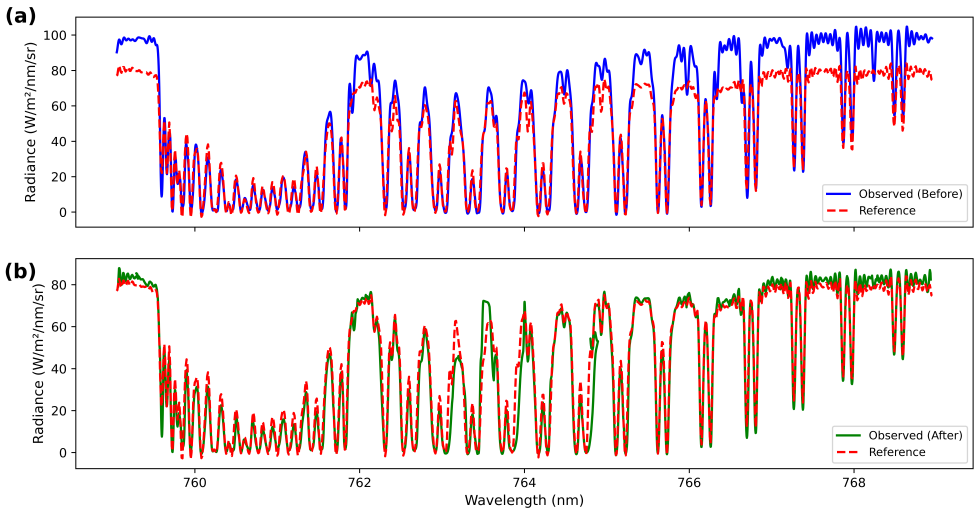


Figure 8. Comparison of O_2-channel radiometric spectra before and after radiometric calibration (Dunhuang, 6 April 2022). (**a**) Original observed spectrum and reference spectrum; (**b**) calibrated observed spectrum and reference spectrum.

After applying the proposed radiometric calibration, the corrected observed spectrum exhibits a substantially improved agreement with the reference spectrum (Figure 8b). The radiance magnitude is effectively adjusted, and the overall spectral shape becomes more consistent with the reference spectrum. Quantitatively, the radiometric response coefficient k decreases from 1.1695 before calibration to 0.9981 after calibration, approaching the ideal value of unity. Meanwhile, the spectral shape consistency represented by R^2 increases from 0.9606 to 0.9738. These improvements demonstrate that the proposed calibration method effectively compensates for radiometric response biases while preserving the original spectral absorption characteristics.

This example further confirms that the proposed radiometric calibration approach can improve the consistency between GMI observations and physically simulated reference spectra under actual observation conditions.

4.4. Multi-Site Validation

To further evaluate the robustness and applicability of the proposed quality improvement framework, additional validation was conducted using GF-5B GMI observations acquired over the Golmud and RRV sites. Compared with the detailed evaluation performed at the Dunhuang site, these two sites represent different observation environments, including a high-altitude arid region and an internationally recognized satellite calibration site. The temporal evolution of the absolute spectral offset, radiometric response coefficient, and spectral shape consistency before and after correction are presented in Figures 9 and 10. The scattered points represent individual observations, while the fitted curves indicate the long-term variation trends of the corresponding quality indicators. The quantitative comparison of the three quality indicators before and after calibration at the two validation sites is further summarized in Table 10.

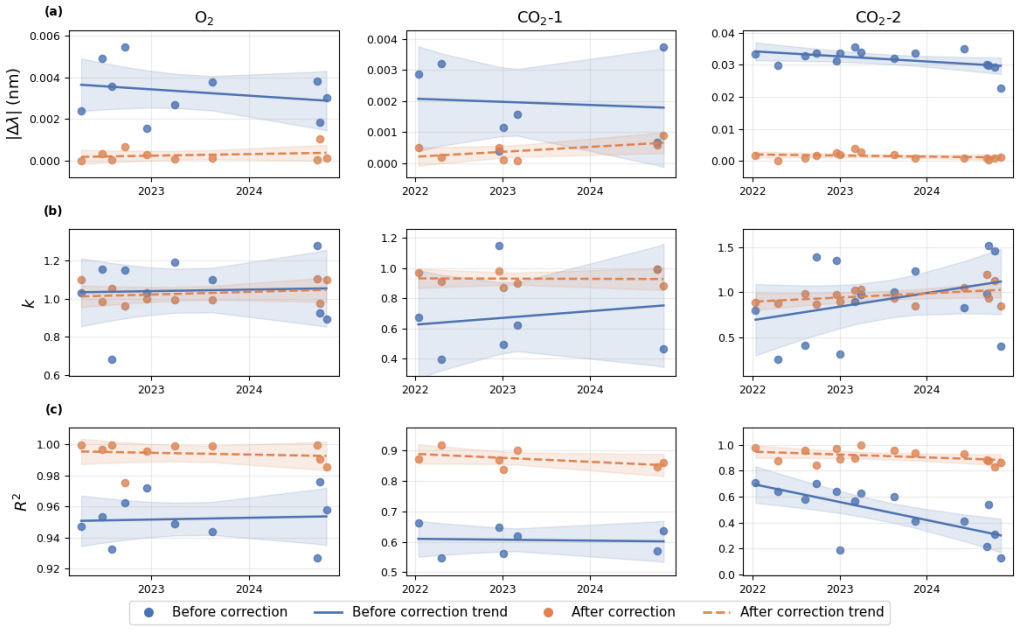


Figure 9. Temporal evolution of quality indicators before and after correction at the Golmud validation site. (**a**) Absolute spectral offset; (**b**) radiometric response coefficient; (**c**) spectral shape consistency.The points represent individual observations, the solid and dashed lines indicate the corresponding linear trends before and after correction, respectively, and the shaded areas represent the approximate 95% confidence intervals of the fitted trends.

Table 10. Quantitative comparison of spectral and radiometric quality indicators before and after calibration at the Golmud and RRV validation sites.

Site	Band	Samples	$\overline{\lvert\Delta\lambda\rvert}$			$\overline{\lvert k-1\rvert}$			$\overline{R^2}$		
			Before	After	Red. (%)	Before	After	Red. (%)	Before	After	Imp. (%)
Golmud	O_2	10	0.003294	0.000265	91.9	0.1429	0.0447	68.7	0.9520	0.9943	4.4
	CO_2-1	7	0.001941	0.000422	78.3	0.3589	0.0711	80.2	0.6058	0.8566	41.4
	CO_2-2	15	0.031804	0.001897	94.0	0.3380	0.1244	63.2	0.4838	0.8854	83.0
RRV	O_2	14	0.003763	0.000939	75.1	0.2897	0.0598	79.4	0.9692	0.9779	0.9
	CO_2-1	10	0.011170	0.000497	95.6	0.5676	0.0983	82.7	0.5188	0.8498	63.8
	CO_2-2	11	0.028040	0.002199	92.2	0.5578	0.1233	77.9	0.4206	0.8534	102.9

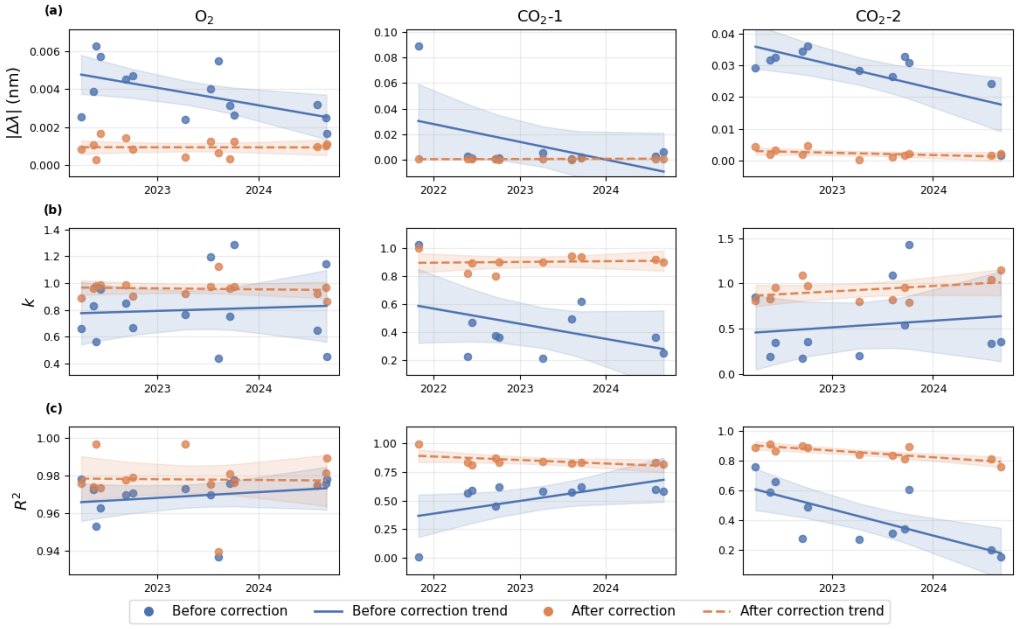


Figure 10. Temporal evolution of quality indicators before and after correction at the RRV validation site. (**a**) Absolute spectral offset; (**b**) radiometric response coefficient; (**c**) spectral shape consistency.The points represent individual observations, the solid and dashed lines indicate the corresponding linear trends before and after correction, respectively, and the shaded areas represent the approximate 95% confidence intervals of the fitted trends.

As shown in Figures 9 and 10, the proposed quality improvement method consistently improves the temporal stability of spectral and radiometric performance across different observation environments. For the spectral offset evaluation, the temporal variations in $|\Delta\lambda|$ before and after spectral recalibration are presented in Figures 9a and 10a. Combined with the quantitative statistics summarized in Table 10, all three absorption bands exhibit reduced absolute spectral offsets after correction at both validation sites. At the Golmud site, the CO_2-2 channel shows the largest spectral offset magnitude before correction, with the mean absolute spectral offset decreasing from 0.031804 nm to 0.001897 nm after recalibration. Similar improvement is observed at the RRV site, where the corresponding offset decreases from 0.028040 nm to 0.002199 nm. The O_2 and CO_2-1 channels also show reduced spectral offsets after correction, indicating improved wavelength consistency. These results demonstrate that the proposed spectral recalibration method effectively reduces wavelength mismatch under different surface and atmospheric conditions.

At both validation sites, the corrected observations exhibit temporal trends closer to the ideal value of one. According to the quantitative statistics summarized in Table 10, the mean $|k-1|$ values decrease after calibration for all absorption bands. For the Golmud site,

the CO_2-2 channel shows relatively large radiometric response deviations before correction, with the mean $|k-1|$ decreasing from 0.3380 to 0.1244 after correction. Similarly, at the RRV site, the mean $|k-1|$ of the CO_2-2 channel decreases from 0.5578 to 0.1233. The O_2 channel requires relatively limited adjustment due to its stable initial radiometric response. These results confirm that the proposed radiometric correction method effectively improves radiometric consistency under different observation environments.

The radiometric response coefficient results are shown in Figures 9b and 10b. Since $k = 1$ represents the ideal agreement between the observed and reference radiance, the deviation of k from unity was used to evaluate the radiometric response consistency before and after correction.

The spectral shape consistency results based on R^2 are presented in Figures 9c and 10c. The temporal evolution of R^2 demonstrates that the proposed quality improvement method enhances the agreement between the measured spectra and the reference spectra. According to the quantitative statistics summarized in Table 10, the R^2 values increase after correction for the CO_2 absorption bands at both validation sites, indicating improved spectral shape consistency.At the Golmud site, the CO_2-2 channel exhibits relatively low spectral shape consistency before correction, with the mean R^2 increasing from 0.4838 to 0.8854 after calibration. A similar improvement is observed at the RRV site, where the mean R^2 of the CO_2-2 channel increases from 0.4206 to 0.8534. The CO_2-1 channel also shows increased R^2 values after correction, while the O_2 channel maintains relatively high R^2 values throughout the observation period due to its inherently stable spectral characteristics. These results confirm that the proposed calibration method effectively improves the spectral shape consistency of GMI observations across different validation sites.

Overall, the multi-site validation results, together with the quantitative statistics summarized in Table 10, demonstrate that the proposed spectral and radiometric quality improvement framework provides consistent performance across different observation environments. Although the initial quality characteristics vary among sites and spectral channels, the corrected observations consistently exhibit reduced spectral offsets, improved radiometric response consistency, and enhanced spectral shape agreement. These results confirm the robustness of the proposed method for improving the in-orbit data quality of GF-5B GMI under different surface and atmospheric conditions.

5. Discussion

The quality degradation of spaceborne hyperspectral instruments during long-term in-orbit operation is generally caused by the combined effects of wavelength instability, detector response variation, and changing observation conditions. Unlike traditional empirical correction methods, the proposed framework establishes a physically constrained relationship between measured GMI observations and simulated radiance spectra by introducing an adaptive reference spectrum library. This strategy reduces the influence of observation condition differences on instrument quality evaluation and enables a more reliable separation of instrumental effects from environmental variability.

The sensitivity analysis demonstrated that surface reflectance and solar zenith angle are the dominant factors affecting the simulated GMI radiance spectra. This result highlights that the radiance measured by GMI is strongly controlled by surface illumination and observation geometry, especially for shortwave infrared greenhouse gas absorption bands. Therefore, using a fixed reference spectrum may introduce additional uncertainties when evaluating long-term instrument performance under different observation conditions. The adaptive reference spectrum approach proposed in this study partially overcomes this limitation by generating observation-dependent reference spectra through parameter inter-

polation. This provides a more physically consistent baseline for spectral and radiometric quality assessment.

The improvement characteristics among different spectral channels further reveal the channel-dependent behavior of GMI instrument performance. The O_2 channel exhibited relatively small initial spectral and radiometric deviations, resulting in limited but stable improvement after correction. This behavior is mainly related to the strong and stable atmospheric absorption features within the O_2 A-band, which provide reliable spectral references for wavelength recalibration. In contrast, the CO_2-1 and CO_2-2 channels showed larger initial inconsistencies because their spectral characteristics are more sensitive to radiometric response variations, instrument stability, and signal changes. Particularly, the CO_2-2 band exhibited the largest improvement in both spectral offset reduction and spectral shape consistency enhancement. This can be attributed to its stronger absorption characteristics and higher sensitivity to spectral response uncertainty, making it more susceptible to wavelength and radiometric deviations during long-term operation.

The multi-site validation results further demonstrate the robustness and transferability of the proposed framework. Although Dunhuang, Golmud, and RRV represent different surface and atmospheric environments, the corrected GMI observations consistently exhibited reduced spectral offsets, improved radiometric response consistency, and enhanced agreement with physically simulated reference spectra. These results indicate that the proposed method is not dependent on a single calibration site and can effectively adapt to different observation scenarios. Therefore, the framework provides a potential solution for long-term monitoring and quality maintenance of greenhouse gas monitoring instruments.

Compared with conventional calibration approaches based on laboratory measurements or solar reference features, the proposed method provides complementary advantages. Pre-launch calibration provides accurate initial instrument characterization but cannot capture temporal changes during orbital operation. Solar Fraunhofer line methods are effective for monitoring wavelength stability but cannot directly address radiometric response degradation. The proposed physics-based approach simultaneously considers spectral and radiometric inconsistencies by combining radiative transfer simulations, instrument response characteristics, and observation-dependent parameters.

Several limitations should also be acknowledged. First, the current reference spectrum library mainly considers clear-sky observations and selected atmospheric parameters; additional atmospheric states and surface types may be required for global-scale applications. Second, the current correction strategy focuses on spectral wavelength shifts and radiometric response deviations, while potential variations in the instrument line shape during long-term operation require further investigation. Future work will extend the reference spectrum library using larger observation samples and evaluate the impact of the corrected radiance products on greenhouse gas retrieval accuracy.

6. Conclusions

This study developed a physics-based spectral and radiometric quality improvement framework for GF-5B GMI observations by integrating an adaptive reference spectrum library, spectral recalibration, and radiometric correction. The proposed framework provides a physically consistent approach to characterize and reduce spectral and radiometric inconsistencies caused by long-term in-orbit operation.

A SCIATRAN-based adaptive reference spectrum library was first constructed by considering observation-dependent parameters, including surface reflectance, solar zenith angle, aerosol conditions, and geographic characteristics. Sensitivity analysis revealed that surface reflectance and solar zenith angle were the dominant factors affecting simulated GMI radiance spectra, while solar irradiance model, atmospheric model, and CO_2 concen-

tration showed relatively limited impacts within the investigated ranges. Based on these results, an adaptive interpolation strategy was developed to generate observation-specific reference spectra.

A joint spectral and radiometric quality improvement method was subsequently proposed. Spectral recalibration based on atmospheric absorption feature matching effectively reduced wavelength-dependent spectral offsets, while radiometric correction using global response coefficients and wavelength-dependent correction factors improved the consistency between observed and reference radiance spectra.

The proposed framework was evaluated using GF-5B GMI observations acquired from September 2021 to December 2024 over Dunhuang, Golmud, and Railroad Valley sites. The results demonstrated that the corrected observations achieved reduced spectral offsets, improved radiometric response consistency, and enhanced spectral shape agreement. Among the three channels, the CO_2-2 band showed the most significant improvement due to its larger initial spectral and radiometric inconsistencies, while the O_2 band maintained relatively stable performance before correction.

Overall, this study provides a physically constrained and transferable solution for improving the in-orbit spectral and radiometric quality of GF-5B GMI Level-1 radiance products. The proposed framework can support more reliable greenhouse gas retrievals and provide a reference for the long-term quality assessment and calibration of future spaceborne greenhouse gas monitoring instruments.

Author Contributions: Conceptualization, H.G. and Y.L.; methodology, H.G., Y.L., Q.W. and B.L.; software, Y.L., Q.W. and B.L.; validation, Y.L., Q.W. and B.L.; formal analysis, Y.L., Q.W. and B.L.; investigation, H.G., Y.L., Q.W. and B.L.; resources, S.L. and G.G.; data curation, H.G., Y.L., S.L. and Q.W.; writing—original draft preparation, Y.L. and Q.W.; writing—review and editing, H.G., Y.L., S.L., Q.W., G.G. and B.L.; visualization, Y.L., Q.W. and B.L.; supervision, H.G., S.L. and G.G.; project administration, S.L. and G.G.; funding acquisition, H.G. All authors have read and agreed to the published version of the manuscript.

Funding: This research was funded by the Jing-Jin-Ji Regional Integrated Environmental Improvement-National Science and Technology Major Project of the Ministry of Ecology and Environment of China (Grant No. 2025ZD1200700). The APC was funded by the research group.

Data Availability Statement: The GF-5B GMI Level-1 data used in this study were provided by the China Centre for Resources Satellite Data and Application (CRESDA) and can be obtained through an application procedure. Due to data access restrictions, the original satellite data cannot be publicly shared.

Acknowledgments: The authors thank the China Centre for Resources Satellite Data and Application for providing the GF-5B GMI data.

Conflicts of Interest: The authors declare no conflicts of interest.

References

1. Intergovernmental Panel On Climate Change (IPCC). *Climate Change 2021—The Physical Science Basis: Working Group I Contribution to the Sixth Assessment Report of the Intergovernmental Panel on Climate Change*, 1st ed.; Cambridge University Press: Cambridge, UK, 2023. [CrossRef]
2. Bruegge, C.J.; Crisp, D.; Helmlinger, M.C.; Kataoka, F.; Kuze, A.; Lee, R.A.; McDuffie, J.L.; Rosenberg, R.A.; Schwandner, F.M.; Shiomi, K.; et al. Vicarious Calibration of Orbiting Carbon Observatory-2. *IEEE Trans. Geosci. Remote Sens.* **2019**, *57*, 5135–5145. [CrossRef]
3. Kuze, A.; Taylor, T.E.; Kataoka, F.; Bruegge, C.J.; Crisp, D.; Harada, M.; Helmlinger, M.; Inoue, M.; Kawakami, S.; Kikuchi, N.; et al. Long-Term Vicarious Calibration of GOSAT Short-Wave Sensors: Techniques for Error Reduction and New Estimates of Radiometric Degradation Factors. *IEEE Trans. Geosci. Remote Sens.* **2014**, *52*, 3991–4004. [CrossRef]

4. Qu, Z.; Jacob, D.; Shen, L.; Lu, X.; Zhang, Y.; Scarpelli, T.; Nesser, H.; Sulprizio, M.; Maasakkers, J.; Bloom, A.; et al. Global distribution of methane emissions: A comparative inverse analysis of observations from the TROPOMI and GOSAT satellite instruments. *Atmos. Chem. Phys.* **2021**, *21*, 14159–14175. [CrossRef]
5. Coldewey-Egbers, M.; Slijkhuis, S.; Aberle, B.; Loyola, D. Long-term analysis of GOME in-flight calibration parameters and instrument degradation. *Appl. Opt.* **2008**, *47*, 4749–4761. [CrossRef] [PubMed]
6. Yoshida, Y.; Ota, Y.; Eguchi, N.; Kikuchi, N.; Nobuta, K.; Tran, H.; Morino, I.; Yokota, T. Retrieval algorithm for CO_2 and CH_4 column abundances from short-wavelength infrared spectral observations by the Greenhouse Gases Observing Satellite. *Atmos. Meas. Tech.* **2011**, *4*, 717–734. [CrossRef]
7. Crisp, D.; Fisher, B.M.; O'Dell, C.; Frankenberg, C.; Basilio, R.; Boesch, H.; Brown, L.R.; Castano, R.; Connor, B.; Deutscher, N.M.; et al. The ACOS CO2 retrieval algorithm—Part II: Global XCO2 data characterization. *Atmos. Meas. Tech.* **2012**, *5*, 687–707. [CrossRef]
8. O'Dell, C.W.; Eldering, A.; Wennberg, P.O.; Crisp, D.; Gunson, M.R.; Fisher, B.; Frankenberg, C.; Kiel, M.; Lindqvist, H.; Mandrake, L.; et al. Improved retrievals of carbon dioxide from Orbiting Carbon Observatory-2 with the version 8 ACOS algorithm. *Atmos. Meas. Tech.* **2018**, *11*, 6539–6576. [CrossRef]
9. Han, Y.; Shi, H.; Li, Z.; Luo, H.; Wang, X.; Ye, H.; Ding, Y.; Zhu, F.; Wu, S.; Xiong, W. On-orbit spectral characteristics analysis of the greenhouse gases monitoring instrument: Spectral wavelength stability and instrumental line shape stability. *Opt. Commun.* **2025**, *574*, 131170. [CrossRef]
10. Shi, H.; Li, Z.; Ye, H.; Luo, H.; Xiong, W.; Wang, X. First Level 1 Product Results of the Greenhouse Gas Monitoring Instrument on the GaoFen-5 Satellite. *IEEE Trans. Geosci. Remote Sens.* **2021**, *59*, 899–914. [CrossRef]
11. Shi, H.; Li, Z.; Ye, H.; Luo, H.; Wang, X.; Xiong, W. Calibration of the Greenhouse Gas Monitoring Instrument (GMI) Based on a Digital Calibration Field Network. *Remote Sens.* **2023**, *15*, 373. [CrossRef]
12. Zhu, F.; Shi, H.; Xiong, W.; Wang, X.; Ye, H.; Han, Y.; Luo, H.; Li, Z.; Cheng, C.; Sun, X.; et al. A Novel Framework for Mixed Noise Removal From Greenhouse Gases Monitoring Instrument (GMI) Interferogram Images on GF5-02 Satellite. *IEEE Trans. Geosci. Remote Sens.* **2024**, *62*, 3432993. [CrossRef]
13. Englert, C.R.; Harlander, J.M.; Brown, C.M.; Marr, K.D. Spatial heterodyne spectroscopy at the Naval Research Laboratory. *Appl. Opt.* **2015**, *54*, F158. [CrossRef] [PubMed]
14. Li, Y.; Wu, H.; Gao, H.; Liu, Q. Evaluation and analysis of on-orbit performance of GF-5B GMI. *Int. J. Remote Sens.* **2026**, *47*, 7430–7453. [CrossRef]
15. Mei, L.; Rozanov, V.; Rozanov, A.; Burrows, J.P. SCIATRAN software package (V4.6): Update and further development of aerosol, clouds, surface reflectance databases and models. *Geosci. Model Dev.* **2023**, *16*, 1511–1536. [CrossRef]
16. Berk, A.; Conforti, P.; Kennett, R.; Perkins, T.; Hawes, F.; Van Den Bosch, J. MODTRAN® 6: A major upgrade of the MODTRAN® radiative transfer code. In *Proceedings of the 2014 6th Workshop on Hyperspectral Image and Signal Processing: Evolution in Remote Sensing (WHISPERS)*; IEEE: New York, NY, USA, 2014; pp. 1–4. [CrossRef]
17. Han, Y.; Shi, H.; Luo, H.; Li, Z.; Ye, H.; Li, C.; Ding, Y.; Wu, S.; Wang, X.; Xiong, W.; et al. Research on Calculation Method of On-Orbit Instrumental Line Shape Function for the Greenhouse Gases Monitoring Instrument on the GaoFen-5B Satellite. *Remote Sens.* **2024**, *16*, 2171. [CrossRef]
18. Zhu, S.; Li, Z.; Hu, X.; Qie, L.; Xu, H.; Qiao, R.; Zhang, Y.; Golry, P. Evaluation and optimal selection of Dunhuang radiometric calibration site based on OLI/Landsat 8 and MSI/Sentinel 2 data. *Int. J. Remote Sens.* **2022**, *43*, 1684–1702. [CrossRef]
19. Hu, X.K.; Gao, H.L.; Cheng, T.H.; Tang, S.H.; Liu, L.; Liu, Q.Y. Site Selection and Evaluation of China's New Radiometric Calibration Test Sites. *Int. Arch. Photogramm. Remote Sens. Spat. Inf. Sci.* **2020**, *42* , 511–520. [CrossRef]
20. Scott, K.P.; Thome, K.J.; Brownlee, M.R. Evaluation of Railroad Valley Playa for use in vicarious calibration. In *Multispectral Imaging for Terrestrial Applications* ; SPIE: Bellingham, WA, USA, 1996; Volume 2818, pp. 158–166. [CrossRef]
21. Zhang, C.; Liu, C.; Chan, K.L.; Hu, Q.; Liu, H.; Li, B.; Xing, C.; Tan, W.; Zhou, H.; Si, F.; et al. First observation of tropospheric nitrogen dioxide from the Environmental Trace Gases Monitoring Instrument onboard the GaoFen-5 satellite. *Light Sci. Appl.* **2020**, *9*, 66. [CrossRef] [PubMed]
22. Kataoka, F.; Crisp, D.; Taylor, T.; O'Dell, C.; Kuze, A.; Shiomi, K.; Suto, H.; Bruegge, C.; Schwandner, F.; Rosenberg, R.; et al. The Cross-Calibration of Spectral Radiances and Cross-Validation of CO2 Estimates from GOSAT and OCO-2. *Remote Sens.* **2017**, *9*, 1158. [CrossRef]
23. Schaaf, C.B.; Gao, F.; Strahler, A.H.; Lucht, W.; Li, X.; Tsang, T.; Strugnell, N.C.; Zhang, X.; Jin, Y.; Muller, J.P.; et al. First operational BRDF, albedo nadir reflectance products from MODIS. *Remote Sens. Environ.* **2002**, *83*, 135–148. [CrossRef]
24. Randles, C.A.; Da Silva, A.M.; Buchard, V.; Colarco, P.R.; Darmenov, A.; Govindaraju, R.; Smirnov, A.; Holben, B.; Ferrare, R.; Hair, J.; et al. The MERRA-2 Aerosol Reanalysis, 1980 Onward. Part I: System Description and Data Assimilation Evaluation. *J. Clim.* **2017**, *30*, 6823–6850. [CrossRef] [PubMed]

25. Buchard, V.; Randles, C.A.; Da Silva, A.M.; Darmenov, A.; Colarco, P.R.; Govindaraju, R.; Ferrare, R.; Hair, J.; Beyersdorf, A.J.; Ziemba, L.D.; et al. The MERRA-2 Aerosol Reanalysis, 1980 Onward. Part II: Evaluation and Case Studies. *J. Clim.* **2017**, *30*, 6851–6872. [CrossRef] [PubMed]
26. Rozanov, V.; Dinter, T.; Rozanov, A.; Wolanin, A.; Bracher, A.; Burrows, J. Radiative transfer modeling through terrestrial atmosphere and ocean accounting for inelastic processes: Software package SCIATRAN. *J. Quant. Spectrosc. Radiat. Transf.* **2017**, *194*, 65–85. [CrossRef]
27. Guo, Y.; Gong, C.; Hu, Y.; Zheng, F.; Liu, Y. On-Orbit Wavelength Calibration Error Analysis of the Spaceborne Hyperspectral Greenhouse Gas Monitoring Instrument Using the Solar Fraunhofer Lines. *Remote Sens.* **2024**, *16*, 3367. [CrossRef]
28. Kang, M.; Ahn, M.H.; Liu, X.; Jeong, U.; Kim, J. Spectral Calibration Algorithm for the Geostationary Environment Monitoring Spectrometer (GEMS). *Remote Sens.* **2020**, *12*, 2846. [CrossRef]
29. Stamnes, K.; Tsay, S.C.; Wiscombe, W.; Jayaweera, K. Numerically stable algorithm for discrete-ordinate-method radiative transfer in multiple scattering and emitting layered media. *Appl. Opt.* **1988**, *27*, 2502. [CrossRef] [PubMed]
30. Saltelli, A.; Ratto, M.; Andres, T.; Campolongo, F.; Cariboni, J.; Gatelli, D.; Saisana, M.; Tarantola, S. *Global Sensitivity Analysis. The Primer*, 1st ed.; Wiley: New York, NY, USA, [CrossRef]
31. Verhoef, W.; Bach, H. Simulation of hyperspectral and directional radiance images using coupled biophysical and atmospheric radiative transfer models. *Remote Sens. Environ.* **2003**, *87*, 23–41. [CrossRef]

Disclaimer/Publisher's Note: The statements, opinions and data contained in all publications are solely those of the individual author(s) and contributor(s) and not of MDPI and/or the editor(s). MDPI and/or the editor(s) disclaim responsibility for any injury to people or property resulting from any ideas, methods, instructions or products referred to in the content.